Acta Materialia 198 (2020) 242–256

Contents lists available at ScienceDirect

Acta Materialia

journal homepage: www.elsevier.com/locate/actamat

Full length article

The thermally activated distortion with amplification effect and related variant selection in red gold alloys

Margaux N.D. Larcher[a,*], Cyril Cayron[a], Andreas Blatter[b], Raphaëlle Soulignac[b], Roland E. Logé[a]

[a] Laboratory of Thermomechanical Metallurgy (LMTM), PX Group Chair, Ecole Polytechnique Fédérale de Lausanne (EPFL), Rue de la Maladière 71b, Neuchâtel 2002, Switzerland
[b] PX Group, Bd des Eplatures 42, La Chaux-de-Fonds 2304, Switzerland

ARTICLE INFO

Article history:
Received 14 April 2020
Revised 21 July 2020
Accepted 28 July 2020
Available online 1 August 2020

Keywords:
Shape memory effect (SME)
Variant selection
Electron backscatter diffraction (EBSD)
Martensitic phase transformation
Order–disorder phenomena

ABSTRACT

Variant selection during the A1→$L1_0$ transformation in a polycrystalline red gold alloy close to equiatomic Au-Cu composition has been extensively studied by Electron Backscatter Diffraction (EBSD) in our previous work. The use of a mathematical description of the lattice distortion and the maximal work criterion allowed us to quantify the degree of selection. With the same approach, we investigate here an interesting shape distortion effect, discovered twenty years ago in equiatomic AuCu-Ga. The shape distortion of thin samples placed in bending condition and then heat-treated under stress is studied in details. The singular shape memory effect and the remarkable distortion amplification, which we call TADA effect, are explored by monitoring the sample radius of curvature and the advancement of the transformation. The underlying mechanisms of variant selection are revealed by EBSD analysis across the samples. The experimental crystallographic variant selection distribution is compared with the expected profile calculated with the Euler-Bernoulli beam theory. The good agreement demonstrates that variant selection during the transformation is at the origin of the macroscopic distortion of red gold alloys. The TADA effect was found to occur when external stresses are released, and strongly depends on the stress at the initial stage of the transformation. This unusual effect is assumed to result from the persistence of variant selection throughout the transformation.

1. Introduction

1.1. Material background

Red gold alloys with compositions close to equiatomic Au-Cu undergo an order-disorder phase transformation A1→$L1_0$ around 410 °C, with short-range diffusion [1], which has been studied since the beginning of the 20th century. The high temperature phase A1 is a disordered f.c.c. (face centered cubic) lattice with random distribution of gold and copper atoms on the crystallographic sites. When slowly cooled from high temperature, the tetragonal distortion of the lattice associated with the ordering of the atoms leads to the AuCuI phase, a f.c.t. (face centered tetragonal) superlattice of type $L1_0$ composed of alternate (002) planes of gold and copper. As the ordering implies diffusion, the transformation can be prevented by water quenching, giving rise to a metastable f.c.c. state at room temperature. Then, increasing the temperature in the f.c.t. stability domain at T ≈ 300 °C, the diffusion increases the kinetics and enables the f.c.c.→ f.c.t. transformation. The kinetics of the transformation depends on several parameters such as the temperature of the prior annealing treatment [2], the temperature of the isothermal ordering treatment, and the previous deformation [3]. The ordering of the Au and Cu atoms leads to a complex microstructure of twin-oriented domains and antiphase boundaries typical of order-disorder transformations [4-6].

1.2. Shape memory effect

A Shape Memory Effect (SME) has been observed in the equiatomic red gold alloy [7], as well as in other $L1_0$-type alloys like FePd and CoPt [8,9]. According to C. Wayman [10], K. Bhattacharya [11] and K. Otsuka [12], the classical SME must involve a martensitic transformation. A comprehensive definition of a martensitic transformation is given by Nishiyama [13]. It is de-

* Corresponding author.
E-mail address: margaux.larcher@epfl.ch (M.N.D. Larcher).

https://doi.org/10.1016/j.actamat.2020.07.064

fined as a displacive transformation, which is a lattice distortion associated with a coordinate motion of atoms. This transformation is often described as diffusionless in the literature, which should consequently exclude the order-disorder transformations. Yet, the presence of an SME in Au-Cu alloys indicates that the A1→$L1_0$ transformation can be both diffusive and displacive. This apparent contradiction is in fact in line with the original definition of the displacive transformation [13], and has been settled long ago for the bainitic transformation [14]. In red gold alloys, the f.c.c. and f.c.t phases are the equivalent of the austenite and martensite phases.

For classical martensitic alloys, the mechanisms of SME are well known [15]. Classical Shape Memory Alloys (SMA) present two main distinct effects at room temperature depending on the range of transformation temperatures. If the martensite finish temperature M_f is above room temperature, the alloy is in the martensitic phase and will behave as a SMA. On the contrary, if the austenite finish temperature A_f is slightly below room temperature, the alloy is in the austenite phase and is superelastic. The initial shape at high temperature is not changed by the phase transformation occurring during the quench. This is due to the self-accommodation of the variants in the material [10]. At room temperature, when sufficient stress is applied, SMA samples deform by the re-orientation of the martensitic variants. When they are heated back above A_f, they come back to their initial shape thanks to the reversibility of the transformation. Alloys undergoing superelasticity have their austenitic phase stable at room temperature. The free energy needed for their deformation is decreased when martensite is formed. Most of the sample deformation is thus accommodated by the formation of some well-oriented stress induced martensite variants. As the martensite is unstable at room temperature, when the stress is released, the material comes back to the austenitic phase. The reversibility of the transformation leads to the original austenite lattice and, thus, to the original sample shape.

These two phenomena rely both on the variant selection of the martensite and on the reversibility of the transformation. The only way to come back to the original shape is to form the original austenitic lattice after the reverse transformation. The reversibility of the A1→$L1_0$ transformation has been proved several times in the literature by the study of the surface relief [7,16]. Similarly, the presence of variant selection in AuCu as well as in FePd and CoPt is well established by the X-ray study of monocrystalline samples under compressive stress [17-19]. More recently, the variants could be detected by Electron Backscatter Diffraction (EBSD) and variant selection could be analyzed and quantified in polycrystalline red gold [20]. This technique has turned out to be very versatile as it measures the degree of variant selection on a large polycrystalline area.

1.3. Thermally activated distortion with amplification effect

In addition to the SME, Ohta and coworkers [7] discovered in $Au_{0.47}Cu_{0.47}Ga_{0.06}$ a very singular shape distortion effect, which has been barely studied so far and has never been reported in any other material. In their work, they wrapped and maintained under stress – around a stainless steel ring – thin lamellae of their alloy, in the austenitic state. They heat-treated the setup to induce the f.c.c. → f.c.t. phase transformation for 5 s at 100 °C, and then they released the lamella from any constraint. At this point, the lamella had almost taken the same radius of curvature as the master ring. They heat-treated again the lamella without applied stress to continue the f.c.c. → f.c.t. transformation, and surprisingly the lamella rolled onto itself. This unexplained effect appears without stress during the heat treatment, and induces a strong amplification of the lamella distortion as compared to the shape initially imposed. The authors did not give name to this phenomenon. Here, we propose to call this effect "Thermally Activated Distortion with Amplification" (TADA). It is different from the classical SME. The deformation under stress may be explained by stress-assisted variant selection, similar to any other shape memory alloy (SMA), but the deformation without stress and the amplification still have to be elucidated. Ohta and coworkers suggested that the variants selected at the initial step of the transformation would continue to grow with the same orientation even if the stress is removed; yet, no evidence has been reported so far. As the link between the variant selection and the TADA effect remains to establish, we decided to investigate in details its connection with the crystallography of the f.c.c.→f.c.t. transformation. In our previous work on red gold alloys [20], we could detect the martensite fct variants by EBSD, and we analyzed and quantified the selection using the maximal work criterion. In the present study, the deformed samples are analyzed with the same procedure, and the variant selection is linked to the amplified shape distortion. The correlation between microscopic variant selection and macroscopic scale TADA effect is confirmed and discussed.

2. Experimental procedure

The mechanical procedure has been performed on three different red gold alloys with a composition close to the equiatomic AuCu. One of this alloy is the standard 5 N alloy with an atomic composition of $Au_{0.51}Cu_{0.43}Ag_{0.06}$. The second and third alloys have platinum and palladium additions, representing less than 6 at%. Such small amount of addition may affect the transformation temperature, the kinetics, the microstructural evolution and the mechanical properties of the alloy, but the nature of the f.c.c. → f.c.t. phase transformation remains unchanged [21-24]. For silver additions, some small amount of silver-rich phase has been reported, but no impact is expected in this work [22,25]. As the result is comparable for the three alloys, only the mechanical results with the third alloy with Pd addition is presented in this work. The microscopic study is performed on the same alloy. Its transformation temperature T_t is close to that of the Au50-Cu50 i.e. around 410 °C.

The material used in this work was cold rolled and thin bands, 400 µm thick, were cut with dimension 150 × 17 mm. The obtained lamellae were recrystallized at 600 °C and water quenched. They are in the f.c.c. state at room temperature and their yield stress is of 380 MPa [20].

In order to apply a stress during phase transformation, the lamellae are manually bent at room temperature in a masterpiece and attached to it in the center with a clamp, in order to make it fit the inner radius of curvature. Six massive masterpieces with different radii of curvature ρ were used to apply different stress levels (Fig. 1a). The initial stress-strain state of the lamellae is estimated with the Euler-Bernoulli beam theory $\varepsilon_x = y/\rho$ with y the distance from the neutral line. The maximal strain is located at the external surfaces. The radii of curvature and equivalent maximal stress-strain are presented in Table 1. The lamella L26 is the only one that undergoes a plastic strain, as the flat shape is not recovered after removing from the masterpiece. According to the stress-strain curve [20], the maximal stress in the lamella L26 is only slightly above the elastic limit for this small strain. The other masterpieces only induce elastic stress, which has been verified by the elastic springback of the lamellae. In addition, a lamella with reduced dimensions F60 (30 × 3 mm) is bent in a four-point bending tool to impose a radius of curvature of 60 mm (Fig. 1b). This device, already used in previous work [26,20], imposes a more precise elastic stress state in the samples for variant selection analysis.

The whole setup (f.c.c. lamella + bending tool) is then heated in a standard furnace at a temperature $T \approx 300$ °C in the f.c.t. sta-

Table 1
Properties of bent lamellae in the different masterpieces. Imposed radius of curvature, maximal imposed stress and strain. F60 has special reduced dimensions 30 × 3 mm. The lamella L26 undergoes plastic strain and its maximal stress is very close to the elastic limit.

Name of the masterpiece	Name of the lamella	Radius of curvature (mm)	Maximal Applied Stress (MPa)	Maximal Applied Strain (%)
***ρ*530**	**L530**	530	40	0.04
***ρ*310**	**L310**	310	68	0.06
***ρ*160**	**L160**	160	132	0.12
***ρ*125**	**L125**	125	170	0.16
***ρ*60**	**L60**	60	353	0.33
***ρ*26**	**L26**	26.5	380	0.75
Four-point bending	**F60**	60	353	0.33

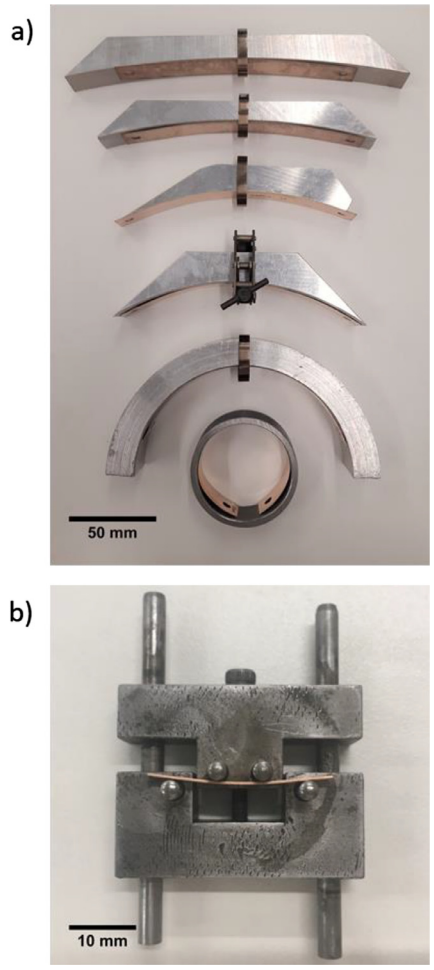

Fig. 1. Bent lamellae before heat treatment. a) Lamellae bent in the six masterpieces b) lamella F60 (dimensions 30 × 3 mm) in the four-point bending device from [26].

bility domain, to enable the f.c.c.→f.c.t phase transformation. As the transformation starts from room temperature, no potential Au-CuII orthorhombic phase can be created and only the f.c.t. phase is formed [1,23,25]. After the heat treatment, the system is cooled down in air to room temperature. The samples are always positioned on their side to avoid any influence of possible creep.

The pictures of the lamellae are always taken at room temperature on a grid paper in order to analyze the distortion. The radii of curvature are approximated in the center and measured by image analysis with the software ImageJ. After the thermomechanical treatments, the lateral cross section of the central part of the lamellae is analyzed. The surface is polished down to 1 µm and electropolished in a solution of 500 ml H_2O, 30 ml H_2SO_4 and 30 ml HCl [27] during 20 s at 27 V. EBSD maps were acquired at 30 kV on a field emission gun scanning electron microscope Gemini 450 (Zeiss) equipped with the Symmetry camera and Aztec acquisition software (Oxford instrument). The step size is chosen as a function of the required statistics and varies between 0.1 and 1 µm. The acquisition rate was of around 300 Hz with detection of 10 bands, with a gain of 2 in the mode speed 1. The hardness measurements are performed with a Qness machine Q10A, with Vickers indenter with loading 100 g for 12 s.

3. Shape changes

3.1. Global behavior

The global behavior of a L125 lamella is detailed in Fig. 2. The lamella is initially flat in the metastable f.c.c. phase at room temperature (Fig. 2a). In a first step, the lamella is elastically bent in the masterpiece ρ125 at room temperature, and maintained with a clamp (Fig. 2b). The system in Fig. 2b is then heated at $T = 320$ °C to induce the f.c.c. → f.c.t. phase transformation. After one hour, the lamella reaches its final shape (Fig. 2c). The final radius of curvature of the lamella is smaller than the one imposed by the masterpiece. The deformation of the lamella is amplified and it goes beyond the simple accommodation; this is the exhibition of the TADA effect. No change is observed upon cooling from 320 °C to 20 °C (Fig. 2c). The lamella is then detached from the masterpiece. The sample, free to move (Fig. 2d), is placed in a furnace at 600 °C for a few minutes to induce the f.c.t. → f.c.c. transformation. After this final annealing, the lamella comes back to its initial flat shape (Fig. 2e). The sample is finally water-quenched to room temperature and remains in its f.c.c. phase (Fig. 2e). The fact that the lamella comes back to its initial shape proves the reversibility of the phenomenon, and thus a SME.

3.2. The TADA effect

To better understand the TADA effect, the evolution of the shape of the lamella is now studied as a function of the heat treatment time. A lamella L26 is bent - with a small plastic deformation - in the masterpiece ρ26 (Fig. 3a) and heated at $T = 280$ °C (this temperature is chosen ≤ 320 °C for achieving a slower kinetics and a better monitoring). After a defined heating time between 0 and 60 min, the setup is quenched in water to stop the transformation and freeze the evolution. The lamella is finally removed from the masterpiece to measure its radius of curvature. Each experiment starts over with a new sample and with a different heating time. This method enables to monitor the shape evolution of the lamella as a function of the heat treatment duration (Fig. 3b). However, the exact kinetics of the phenomenon cannot be analyzed since the samples are placed in the masterpiece at room temperature for practical reasons, and not at the target temperature. The same experiment has been performed with a masterpiece preheated at 280 °C, and the kinetics was significantly increased, but the final shape was not affected.

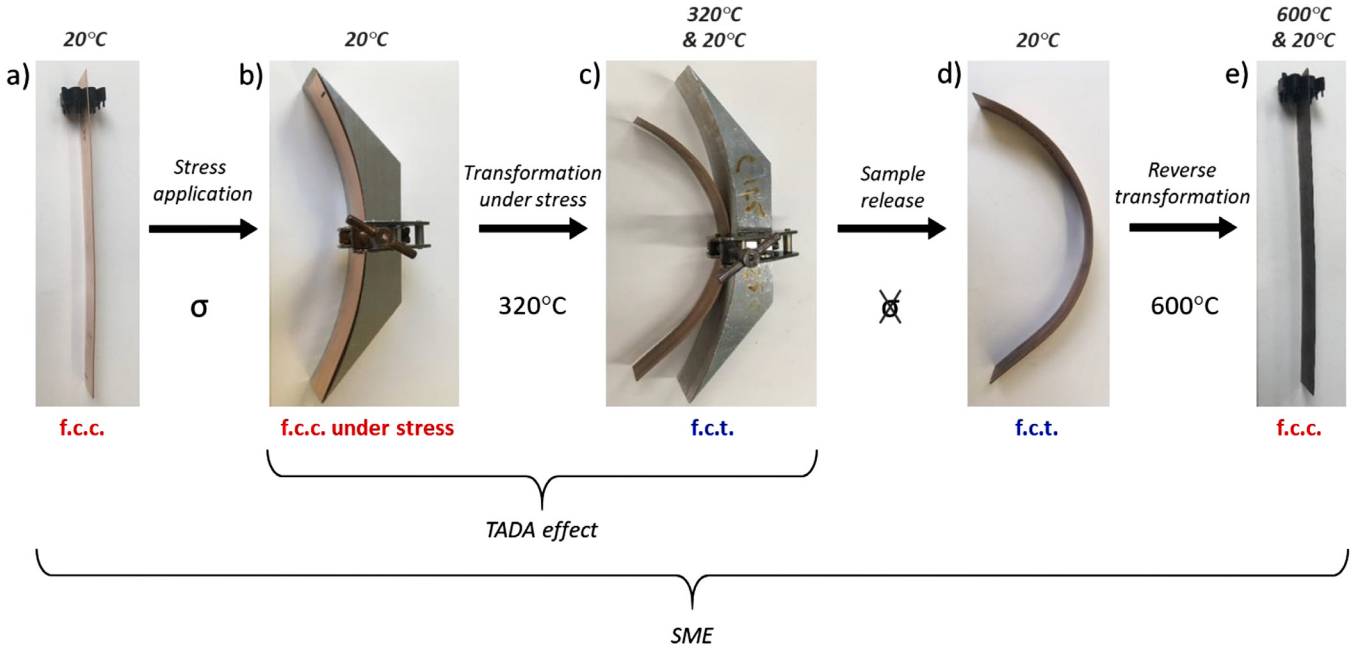

Fig. 2. Detailed behavior of the L125 lamella exhibiting intricate TADA effect and SME. a) Initial lamella in the f.c.c. phase at room temperature b) bent in the masterpiece ρ125 at room temperature c) heat-treated under stress at 320 °C for 60 min d) released from the masterpiece e) heat-treated at 600 °C for a few minutes.

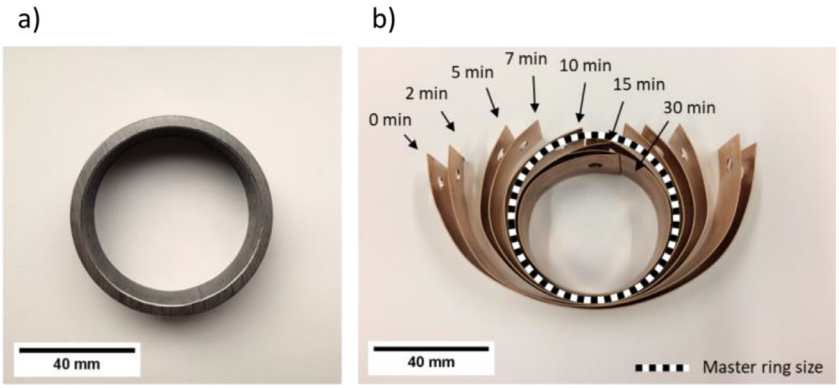

Fig. 3. a) Masterpiece ρ26 b) Several L26 lamellae placed in the masterpiece at room temperature and heat-treated in the masterpiece for different durations at $T = 280$ °C.The hatched circle represents the masterpiece size for a visual reference.

Fig. 4a shows the evolution of the radius of curvature of the lamella compared to the initial radius of curvature. The radius of curvature of the masterpiece is in dotted lines. The initial radius of curvature of the sample at t = 0 min is due to the plastic deformation induced by the bending in the masterpiece. After 10 min in the furnace, the lamella reaches the radius of curvature of the masterpiece. The lamella can be removed with no effort from the masterpiece, which confirms that the lamella is not under stress anymore. For longer heat treatments, the radius of curvature of the lamella continues to decrease beyond the deformation imposed by the masterpiece, until it reaches its final shape (TADA effect).

In a first approximation, the strain in the sample is supposed to be comparable to that of a lamella elastically bent with the same radius of curvature. The strain in the samples is estimated with the formula $\varepsilon_x = y/\rho$. The evolution of the maximal strain (situated at the surfaces for $y = 200$ µm) is presented in Fig. 4b. In this experiment, the evolution of the transformation is also monitored by measuring the hardness at room temperature. The hardness of the f.c.t. phase being higher than that of the f.c.c. phase, it can be considered as an indicator of the advancement of the transformation [5]. The hardness of the f.c.c. phase of this alloy is 170 Hv0.1. It indicates 0% of transformation. The maximal value of hardness measured in this study is 322 Hv0.1. It stands for the 100% transformation. Fig. 4.b shows the evolution of hardness and maximal strain as a function of the heating time. The two curves have a very similar evolution; Fig. 4c shows a linear relationship between them. The macroscopic deformation of the lamella is thus linked to the f.c.t. phase formation. In Fig. 4b, one can note that when the lamella reaches the masterpiece shape after 10 min, the transformation is not maximal. The hardness and the strain have reached close levels i.e. respectively 64% and 71% of their maximal measured values. As the transformation goes on without stress, the sample continues to deform proportionally to the amount of formed martensite, until the maximum is reached.

3.3. Influence of the initial stress

In Ohta et al. previous work [7], the impact of stress on the shape changes was not clearly elucidated, because the samples were slightly plastically deformed. In this study, the fact that the yield stress is not reached in most of the samples indicates that the mechanism of variant selection is stress-assisted, at least in its initial stage. For that reason, the influence of the applied stress on the shape change has to be studied. For this purpose, the lamellae are

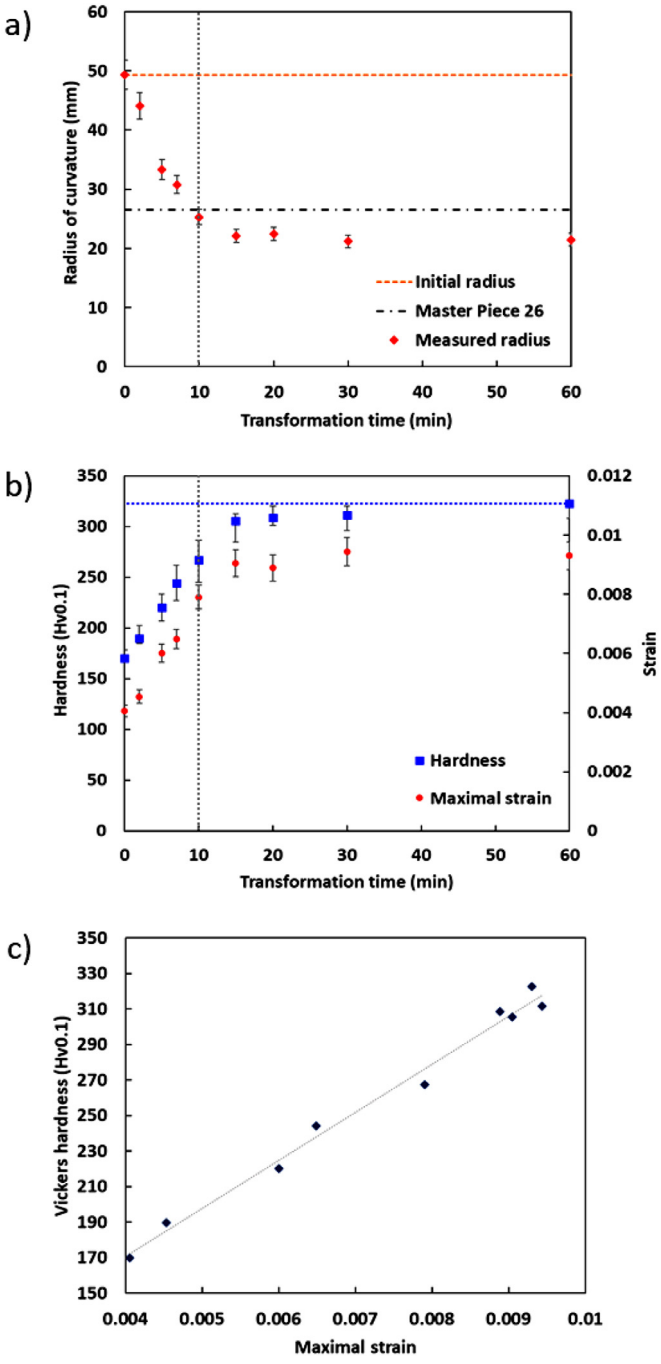

Fig. 4. Evolution of the lamella L26 shape with the heat treatment duration at 280 °C a) Radius of curvature with error bars of 5% b) Maximal strain with error bars of 5% and hardness with error bars representing the minimum and maximum of the 10 measurements c) Linear fit of hardness versus maximal strain.

bent in the different masterpieces and transformed under stress for 1 h at $T = 320$ °C, to reach their final shape. After the transformation, the distortion caused by the transformation is plotted as a function of the initial stress in Fig. 5. The black dashed line represents the initial elastic strain imposed by the masterpiece radius of curvature.

The final strain induced by the phase transformation linearly depends on the initial stress in the elastic domain; the higher the initial stress, the higher the final strain. If the shape was only due to stress-assisted variant selection, the lamella would have taken the imposed radius of curvature to release the stress, and the final shape would be that of the black dashed line in Fig. 5, corresponding to $\sigma = 0$. However, the final strain goes *beyond* the $\sigma = 0$ line: this is the TADA effect. One can note that the gap between the stress-assisted variant selection line and the final strain of the lamellae is roughly independent of the stress, and represents about 0.2% strain. In the plastic domain, however, the behavior does not seem to follow anymore the elastic trend. The final strain induced by the transformation is lower than predicted by the trend extrapolation (the initial plastic strain being subtracted). This result might come from the limited accuracy of the measurement, but it might also indicate that plastic deformation tends to inhibit the variants selection and the TADA effect. As the transformation occurs first under stress and then without stress, the terms *extension* and *contraction* will refer to positive and negative deformation, respectively, regardless of the presence of stress.

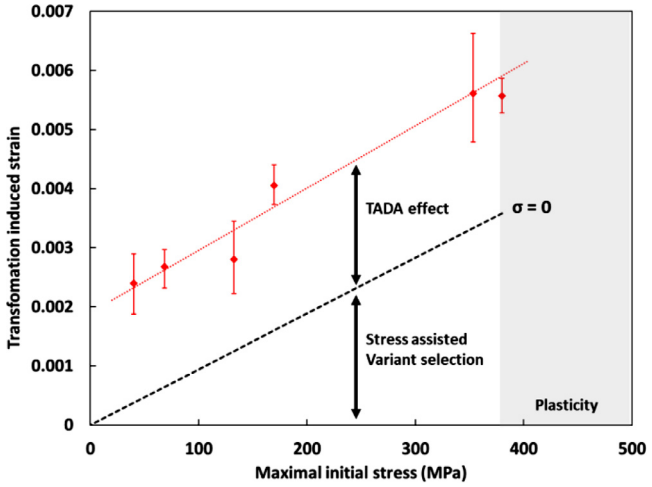

Fig. 5. Evolution of the maximal strain induced by the transformation (value on the external surfaces of the lamellae) after 1 h at 320 °C, as a function of the initial stress applied before the transformation and linear fitting with red line. The shaded area represents the zone where the initial stress is higher than the elastic limit. In black dashed line, the hypothetical case of a simple accommodation of the imposed shape by stress-assisted variant selection, leading to a stress free state. The error bars represent the minimum and maximum of the twelve measurements. (For interpretation of the references to colour in this figure legend, the reader is referred to the web version of this article.)

4. Variant selection

4.1. Degree of variant selection calculation

In our previous work [20], the variant selection in polycrystalline samples was successfully analyzed by EBSD. The distortion matrix in the sample reference frame was calculated from the experimental Euler angles and the c/a ratio. Then the lattice strain tensor $\boldsymbol{\varepsilon^I}$ of the formation of each variant was calculated, and its mechanical work of formation $W = \boldsymbol{\sigma} : \boldsymbol{\varepsilon^I}$ with σ the initial applied stress tensor (local and global stress tensors are assumed to be equivalent). The selection could be successfully analyzed by the maximal work criterion, which states that variants associated with high work are easier to form and, thus, more present. A quantification method was proposed for the degree of variant selection τ with Eq. (1):

$$\tau = \frac{\bar{W} - \bar{W}_{equi}}{\bar{W}_{max} - \bar{W}_{equi}} \quad (1)$$

The work $\bar{W}$ is the average work of all variants actually detected by EBSD. $\bar{W}_{equi}$ is the average work in the hypothetical case of an equi-repartition of all three possible variants within each f.c.c. grain. $\bar{W}_{equi}$ is non-zero because of the volume change during the

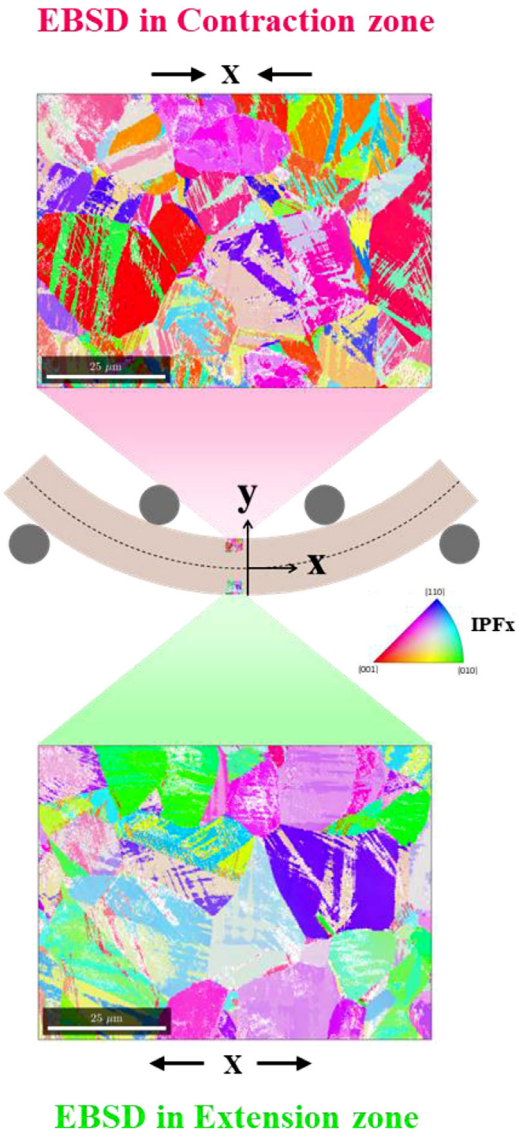

Fig. 6. Schematic representation of the four-point bending test with variant selection in the extension and contraction areas, shown from EBSD map in IPFx coloring. Adapted from [20]. (For interpretation of the references to colour in this figure legend, the reader is referred to the web version of this article.)

transformation. $\bar{W}_{max}$ is the average work in the hypothetical case where only the variant with the maximal work is formed within each grain. The degree of section τ varies between 0, in the case of no variant selection, and 1 for the maximal variant selection.

According to the Euler-Bernoulli theory, the circular bending of a beam gives rise to a very simple stress state with no shear and a constant bending moment, which does not exactly reflect the reality especially for large distortions. However, due to the significant experimental error in the manual bending tests (Fig. 5), this simple model will be used for the analysis of the variant selection in a first place. In this specific case of simple unidirectional loading along x, the mechanical work is simply given by $W{=}\varepsilon_x\,\sigma_x$. In the zones where the initial stress is tensile, the variants with highest W give rise to an extension of the lattice in the x direction upon transformation; inversely, in the zones where the stress was initially compressive, selected variants give rise to a contraction of the lattice in the x direction. This difference in crystallographic orientation of the lattices is observed on the EBSD maps in IPFx coloring, as depicted in Fig. 6. Maps with variant selection in contraction are red, while those in extension are blue and green.

Thanks to the simplification of the work calculation for unidirectional loading, Eq. (1) can also be expressed in terms of the average *lattice* strain along the loading direction in Eq. (2). All the strains referred thereafter correspond to the component along the loading direction x.

$$\tau^l = \frac{\bar{\varepsilon}^{\,l} - \bar{\varepsilon}^{\,l}_{equi}}{\bar{\varepsilon}^{\,l}_{max} - \bar{\varepsilon}^{\,l}_{equi}} \tag{2}$$

If the distortion of the lamella is only due to variant selection, we assume that the *macroscopic* strain ε^{m}, is equal to the average *lattice* strain, $\varepsilon^m = \bar{\varepsilon}^{\,l}$. The macroscopic strain can be computed from the final radius of curvature of the lamellae. Therefore, a macroscopic estimation of the variant selection degree τ^{m} can be calculated from the observed final macroscopic strain ε^{m}:

$$\tau^m = \frac{\varepsilon^m - \varepsilon^m_{equi}}{\varepsilon^m_{max} - \varepsilon^m_{equi}} \tag{3}$$

In Eq. (3), the reference strain in the equi-repartition case ε_{equi} corresponds to the strain in absence of variant selection. It is one third of the isotropic volume change of the material during the transformation and $\varepsilon^m_{equi} = \bar{\varepsilon}^{\,l}_{equi}$. The value is calculated from the lattice parameters given in [20] and amounts to −0.26%. The strain in the case of a maximal variant selection ε_{max} is different in extension and in contraction, and it depends on the orientation of the parent f.c.c. grains. In this study, the initial material is not textured (see Appendix A). In order to calculate ε_{max} in a polycrystal, 10,000 random f.c.c. grain orientations were generated with Matlab, and the strain of the variant with highest W was computed in tension as well as in compression, in each grain. The average strain along the loading direction x obtained in both cases give rise to $\bar{\varepsilon}^l_{max} = 1.12\%$ in extension and $\bar{\varepsilon}^l_{max} = -2.24\%$ in contraction.

4.2. Macroscopic expected degree of selection

In this section, the degree of variant selection is estimated from the macroscopic observation of the lamellae with two models. For this purpose, the lamella with the highest initial stress L60 is analyzed. After transformation for 1 h at 320 °C, the final shape corresponds to that given in Fig. 5 for an initial maximal stress of 350 MPa.

The first model is based on the observed final shape of the lamella. As in Section 3.2, the macroscopic strain profile is computed by assuming it is equivalent to the strain in a lamella elastically bent with the same radius of curvature. The strain profile across the lamella schematically represented in Fig. 7a is calculated from the radius of curvature after the transformation, and plotted in Fig. 7b in plain line. The corresponding expected degree of variant selection τ^{m} calculated from Eq. (3) is plotted in plain line in Fig. 7c with variant selection in extension and compression respectively displayed in green and red.

The second model is rather based on the TADA effect considering the initial stress state in the lamella. Indeed, one can note that the law, which links the initial stress and the final strain in Fig. 5, is affine and not merely linear, as it does not intercept the strain axis at zero. This implies that for an initial stress close to zero, the strain due to the TADA effect is non-zero (even a very slight stress level makes the lamellas bend). The curve in Fig. 5 is fitted and then applied to the initial stress profile in the lamella F60 computed with the Euler-Bernoulli theory. The strain profile expected with this second model is plotted in dotted line in Fig. 7b. The corresponding degree of variant selection is plotted in dotted line in Fig. 7c.

In any case, during the transformation, the stress in the sample is released. The zone above the neutral line initially in tension

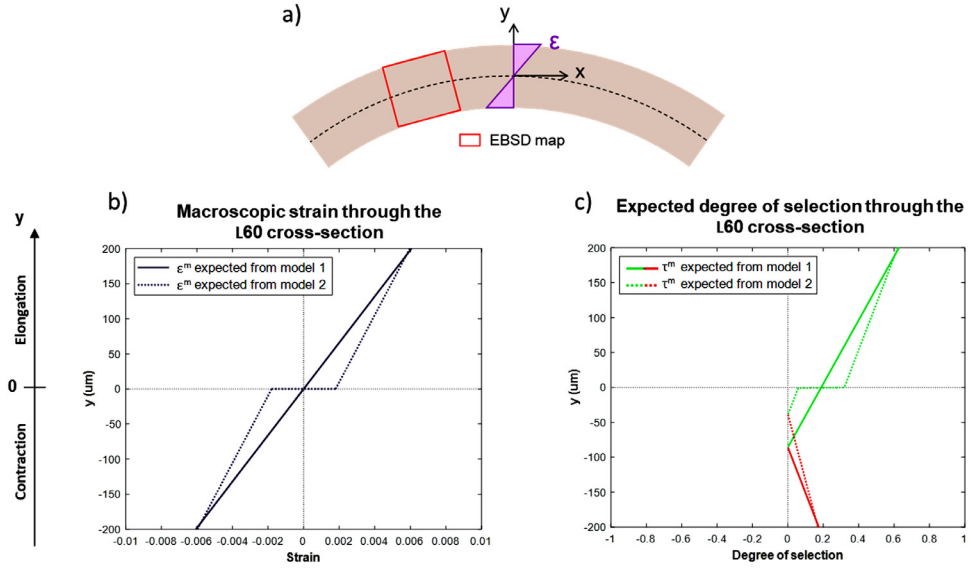

Fig. 7. a) Schematic representation of the cross section of the lamella L60 after transformation at 320 °C for 1 h, with the schematic strain profile in purple and EBSD maps area in red. b) Macroscopic strain ε^m evolution across the sample calculated with the two models, c) corresponding expected degree of variant selection τ^m across the sample section, calculated from ε^m. The variant selection in extension is in green and that in contraction is in red. (For interpretation of the references to colour in this figure legend, the reader is referred to the web version of this article.)

presents an elongation along x after the transformation, and the zone under the neutral line initially in compression presents a contraction along x. For $\varepsilon = 0$, some extension variants are selected to accommodate the negative volume change of the lattice occurring during transformation (see Eq. (2)). As the neutral line is supposed invariant, the expected degree of selection at y = 0 is thus positive in both cases. The maximal expected amount of variant selection is 0.58 at the maximum of extension, and 0.15 at the maximum of contraction (same for both models).

4.3. EBSD analysis

In order to compare the macroscopically expected degree of variant selection τ^m with the microscopic measured one τ^l, the cross section of lamellae is characterized by EBSD for determining the variant selection. Two lamellae with high initial elastic stress were extensively studied, L60 and F60. In total, more than ten maps were performed across the whole section of the lamellae, as depicted in Fig. 7a. In our previous work, the f.c.c. grains were reconstructed with the software ARPGE [28]. Yet, thanks to the very close lattices of the parent and daughter phases, it is possible to easily reconstruct the grains with Matlab by re-assigning the Euler angles of the present f.c.t. phase to the prior f.c.c. crystals, and that is the method we used in the present study. A part of one of the EBSD maps is represented in Fig. 8 (the full map is in Appendix B). A step size of 1 µm was chosen to measure a sufficient number of grains orientations for being statistically representative, leading to an acquisition time of about 1 hour. Some EBSD maps were also acquired with a smaller step size on a narrower area; they gave similar results, with more statistical noise. The data is treated with the same process as detailed in our previous work [20]. Only the 3 stretch variants are considered as an approximation of the 12 distortion variants that are possibly formed in the material. This approximation is possible because the rotational part of the polar decomposition is small (rotation angle = 1.56°) and does not affect significantly the work W. They are represented by the distortion matrices calculated from the Euler angles. The strain tensor of each variant is defined by $\boldsymbol{\varepsilon}_{/s} = D_{/s} - \mathrm{Id}_{/s}$ in the sample basis *S*.

The reconstructed f.c.c. grains shown in Fig. 8a present a noticeable size heterogeneity across the sample. This type of microstructure has been observed in several samples. This is due to the previous processing of the sample, and it is supposed to have no impact on the studied phenomenon. Fig. 8b shows the f.c.t. domains in IPFx colors. On the elongation side above the neutral line, the f.c.t. grains are mainly blue and green, which corresponds to domains with their contraction axis away from the tensile direction. In the contraction area, the f.c.t. grains are mainly reddish, which corresponds to domains with their contraction axis close to the compressive direction. This is consistent with the expected repartition of variants [20]. In Fig. 8c, the color is a function of ε^l, the x-component of the strain matrix of each variant. The red color is attributed to the variants that are deformed in extension in the x direction, while blue indicates contraction. This color coding makes clearer the variant selection on both sides of the neutral line, with mainly red variants above, and more blue variants below the neutral line.

The quantitative evolution of variant selection along the y axis can now be compared to the macroscopic profile expected from the two models, in Fig. 9. For each coordinate y, $\bar{\varepsilon}^l$ the average x-component of the lattice strain of the f.c.t. variants and τ^l the corresponding degree of selection, are computed and compared to the profiles of Fig. 7. The calculation is performed on the 7700 reconstructed f.c.c. grains of the full map in appendix Fig. B.1.

The average lattice strain in the loading direction x, $\bar{\varepsilon}^l$, determined from the EBSD map is positive in the upper part of the cross section and negative in the lower part, as expected. Taking into account the statistical noise, the degree of selection τ^l calculated from the EBSD data is in relatively good agreement with the expected distribution τ^m calculated from both models. In addition, the extremum values fit the expectations. One can also note that the experimental inversion point were the variant selection switches from extension to contraction is close to the value expected from the first model. However, the neutral axis seems to be shifted to the contraction side of the sample. The strain measured in the EBSD map and the degree of variant selection is higher than expected in the elongation part. This shifting might be due to the presence of a very small amount of plastic deformation in the L60. The existence of a small difference on the yield stress in tension and compression (of about 40 MPa) might cause an asymmetry in the initial stress profile.

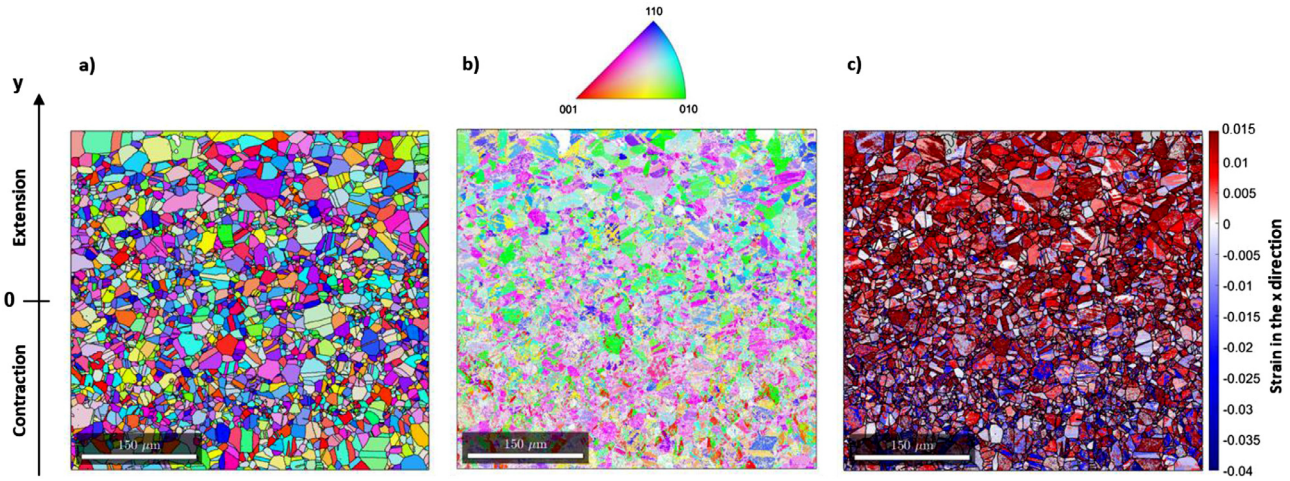

Fig. 8. EBSD map of the cross section of sample L60 in the zone depicted in Fig. 7a, after transformation at 320 °C for 1 h. Subset map of the appendix Fig. B.1. a) Reconstructed f.c.c. parent grains in IPFx coloring b) f.c.t. variants in IPFx coloring c) the f.c.t. variants colored according to the corresponding lattice strain in the x direction ε^{l}. (For interpretation of the references to colour in this figure legend, the reader is referred to the web version of this article.)

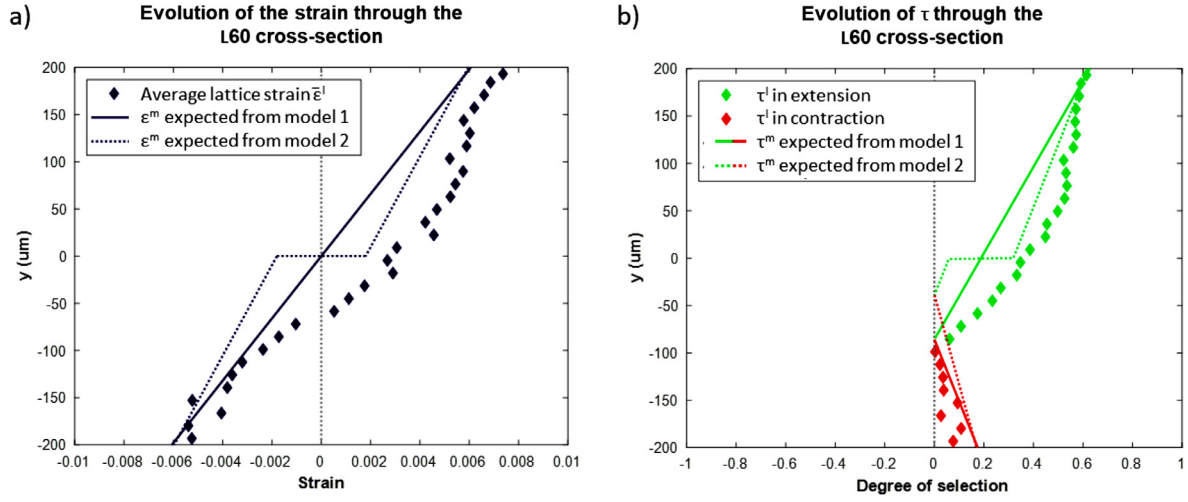

Fig. 9. Evolution of variant selection along the cross section of L60 after transformation. Calculated from the map in appendix Fig. B.1a) Comparison between the microscopic average strain in the x direction, $\bar{\boldsymbol{\varepsilon}}^{\boldsymbol{l}}$, calculated from the lattice strains measured in the EBSD map, and the macroscopic expected strain profiles of ε^{m} from Fig. 7; computed with the two models. b) Degree of variant selection τ^{l} calculated from the EBSD data, and τ^{m} expected from ε^{m}. Extension selection in green and contraction selection in red. (For interpretation of the references to colour in this figure legend, the reader is referred to the web version of this article.)

Overall, this discrepancy in strain might be explained by the fact that initial states of stress in the lamellae bent in the masterpieces (Fig. 1a) were not exactly that expected from the models. In order to obtain a more reliable stress profile for a quantitative comparison, the masterpiece ρ60 was replaced by the four-point bending tool with an imposed radius of curvature of 60 mm. The EBSD map performed on the cross-section of the sample F60 after transformation for 1 h at 320 °C is shown in Appendix C. The result of the analysis of the 10 400 reconstructed f.c.c. grains is presented in Fig. 10.

In this bending condition, the microscopic strain and variant selection are both in better agreement with the macroscopic distribution expected from the two models. In particular, the strain crosses the zero much closer to the neutral line. The inversion point where the variant selection switches from extension to contraction is now in very good agreement with the second model. One can note that the experimental data always display an S-shape curve (Fig. 9, Fig. 10, and supplementary material). This S-shape trend is well explained by the second model. In the central part of the sample, the experimental data are closer to the first model. Finally, it appears that the experimental strain and variant section distribution lie in-between the two proposed models. The very good fitting between the measured variant selection and the one expected from the macroscopic observations confirms that the shape distortion is well explained by the variant selection of the f.c.t. phase during the transformation

5. Discussion

Our EBSD analysis demonstrates the link between the macroscopic behavior of the alloy and the microscopic variant selection at the origin of the TADA effect. The final shape of the lamella is entirely due to the selection of f.c.t. variants. This result is also confirmed by the almost perfect shape recovery of the lamella when getting back to the f.c.c. phase (Fig. 2e). The link being properly established, the underlying mechanisms can be discussed.

As mentioned previously, the behavior of this alloy differs from the classical behaviors observed in shape memory alloys. Usual superelasticity and SME are schematized in Fig. 11a and b, respectively. In both cases, the intermediate deformed shape is obtained by the accommodation of the imposed strain with martensite variants. In standard SME, the martensite is stable at room tempera-

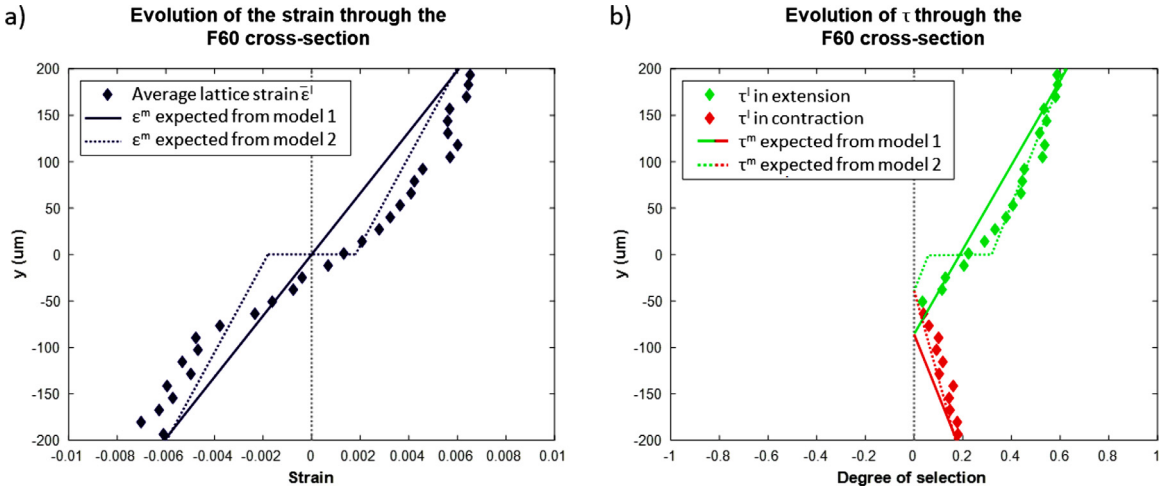

Fig. 10. Evolution of variant selection along the cross section of F60 after transformation. Calculated from the map in appendix Fig. C.1a) Comparison between the microscopic average strain in the x direction, $\bar{\varepsilon}^{l}$, calculated from the lattice strains measured in the EBSD map, and the macroscopic expected strain profiles of ε^{m}; computed with the two models. b) Degree of variant selection τ^{l} calculated from the EBSD data, and τ^{m} calculated from the two different ε^{m} of figure a. Extension selection in green and contraction selection in red. (For interpretation of the references to colour in this figure legend, the reader is referred to the web version of this article.)

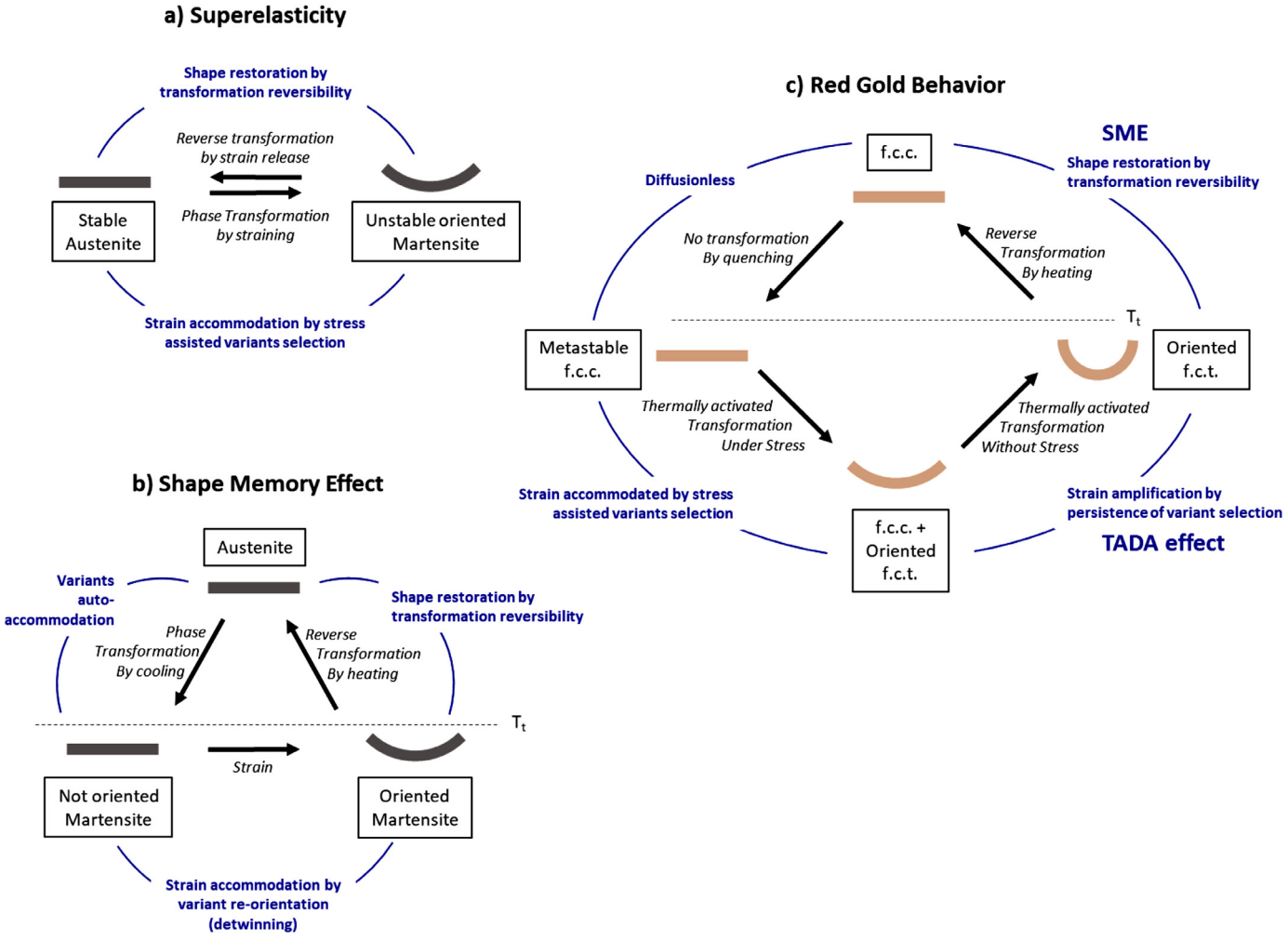

Fig. 11. Schematic view of the classical behaviors a) superelasticity b) shape memory effect; and comparison with c) the red gold alloys behavior.

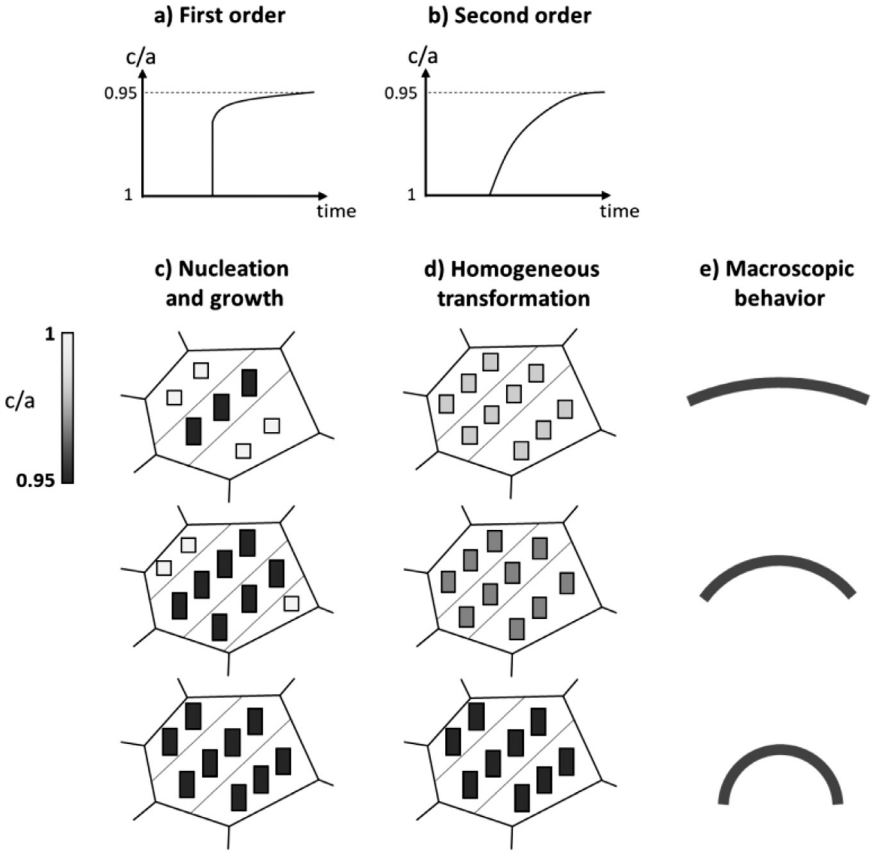

Fig. 12. Evolution of the c/a ratio if the transformation is of a) First order b) Second order. Schematic view of the two possible transformation mechanisms. c) Classic nucleation and growth with well-defined c/a ratio, d) Homogeneous transformation with gradual lattice distortion. e) Schematic corresponding macroscopic behavior.

ture and the strain imposed to the material is accommodated by re-orientation / detwinning of the martensite variants (Fig. 11a). For superelasticity, the strain is given by the formation of well-oriented martensite variants under stress (Fig. 11b).

As a comparison, the sequence of the distortion behavior of the red gold alloy is depicted in Fig. 11c. The initial lamella is in its austenite f.c.c. phase (metastable) obtained by water quenching from high temperature. As the formation of the f.c.t. phase is diffusion-limited, the distortion is achieved by a heat treatment. In a first step during the heat treatment in a masterpiece, the imposed stress is released by stress-assisted variant selection. If one considers only the phases, this mechanism is comparable to that of superelasticity, but here the mechanism is thermally activated and without immediate reversibility. In the second step of heat treatment, although the stress has been fully released, the macroscopic distortion continues until the end of the transformation. This TADA effect can only be explained by the persistence of the variant selection initiated under stress at the previous step until the end of the transformation. The final shape recovery is based on the reversibility of the phase transformation, as in a classical SME.

We could observe the same global behavior described in the Fig. 11c in the three different red gold alloys previously mentioned. This indicates that it might be a general behavior of red gold alloys undergoing the $A1 \rightarrow L1_0$ transformation. In addition, the inhibition of the TADA effect (Fig. 5) by the plastic strain is also observed in the other red gold alloys.

Contrary to classical shape memory alloys, the $A1 \rightarrow L1_0$ transformation is not instantaneous and the lamella continues to bend until the transformation reaches a maximum (Fig. 4). One can conclude that the diffusional aspect of the transformation is at the origin of the phenomenon. Our EBSD analysis shows that the shape going beyond the imposed radius of curvature is due to variant selection continuing with the same trend, even when the stress is released. In this case, the final shape would depend mainly on the c/a ratio. Similar experiments with alloys with very different c/a ratios could prove this hypothesis. As the persistence of the variant selection during further transformation, even after releasing the stress, has already been shown in FePd monocrystals [18], the same sequence of distortion is also expected in FePd and CoPt undergoing the same transformation. The same persistence is also observed when the variant selection is performed by means of electric field [19].

The fact that the variant selection continues even when there is no stress anymore indicates that the initiation of the transformation is of high importance. The dominant influence of initial stress on further variant selection has previously been shown by Ichitsubo et al. in their XRD study of FePd monocrystals [18,19]. In this work, we showed that the final deformation linearly depends on the initial stress. The higher the stress, the higher the distortion and consequently, the higher the variant selection (Fig. 5). We also showed that the TADA effect is responsible for an amplification of 0.2% strain, as compared to the simple stress-assisted variant selection. Most importantly, Fig. 5 shows that, thanks to the TADA effect, a significant deformation can be induced by the application of a low stress level, e.g. a process induced residual stress. Indeed, the application of 40 MPa gives rise to a strain more than 6 times higher than in the case of pure stress-assisted variant selection. The variant selection during the transformation under residual stress might explain the odd shape behavior of very thin lamellae transformed without external stress in [7,29], or the

macroscopic distortions of bars during industrial processing [3]. Further study on the influence of stress during the early stages of the transformation will give more indications on the level of stress needed for initiating variant selection (<40 MPa).

The TADA effect can be attributed to two possible mechanisms, depending on whether the transformation is of first or second order. The two cases are schematically depicted in Fig. 12.

If the transformation is of first order and occurs by nucleation and growth, the order parameter (here c/a ratio) presents a discontinuity as shown Fig. 12a. In this case, the persistence of variant selection during the transformation could be explained by an autocatalytic phenomenon. The presence of a particular f.c.t. precipitate would induce stresses in the f.c.c. matrix favoring the subsequent nucleation and growth of the same variant in the surrounding region (Fig. 12c). This hypothesis was supported by Ichitsubo et al. [30] and their calculations, based on the continuous theory of Eshelby and the lattice distortion. Nevertheless, another characteristic of shape memory alloys is the auto-accommodation of the variants. In the case of AuCu, it usually gives rise to alternate oriented variants and to a typical "twinned" microstructure when no stress is applied [4]. This mechanism appears to accommodate the local stress induced by the f.c.c. lattice distortion. Although this characteristic may seem inconsistent with an autocatalytic mechanism, auto-accommodation and the autocatalytic mechanisms could appear within the same phase transformation, similar to autocatalytic lenticular martensite presenting nano-twinned midrib [31].

The alternative hypothesis would rely on a second-order character of the transformation. In that case, the c/a ratio would gradually decrease from 1 to 0.95 (Fig. 12b) during the heat treatment. In this idealized view, the transformation would be homogeneous, all the volume would start to transform at the same time with a very small c/a distortion, as schematically represented in Fig. 12d. In the first step of the transformation, all variants would be selected by the initial stress, and the progressive evolution of c/a could fully explain the progressive shape distortion inducing the TADA effect (Fig. 12e), regardless of the subsequent stress state.

Whether the f.c.c.→ f.c.t. transformation in red gold alloys is of first order and implies a nucleation and growth mechanism, or is of second order and instantaneously occupies the whole volume, is not clearly established in the literature [32,33]. DSC (differential scanning calorimetry) curves of red gold alloys exhibit a small exothermic peak during the ordering [34,35], which is an indication of a first order transformation. Yet, a gradual shift of the f.c.t. phase peaks in X-ray diffraction has already proved the possibility of a gradual evolution of the c/a ratio [36]. The two schematic hypotheses of Fig. 12 are extreme cases. Actually, perfectly second order transformations are rarely observed when measurements are done with high accuracy. Other experiments (not published yet) tend to show that both mechanisms are implied, and that the TADA effect should result from the diffusion-limited and weak first-order characters of the transformation.

Conclusion

In this work, a singular shape distortion and related variant selection has been studied in a red gold alloy, via bending experiments and subsequent heat treatments around 300 °C, inducing the f.c.c. → f.c.t. transformation under stress.

1) During the first step of the heat treatment, distortion occurs under stress by thermally-activated stress-assisted variant selection until the stress is released and the strain is accommodated.
2) Despite the stress release, the distortion of the lamella continues during the heat treatment. This very special behavior was named Thermally Activated Distortion with Amplification (TADA) effect. Our study showed that the TADA effect is due to the persistence of variant selection until the end of the transformation.
3) The TADA effect was proved to depend affinely on the initial level of applied stress at the beginning of the phase transformation with an offset of around 0.2% strain. Very small stresses (around 40 MPa) give rise to a considerable strain amplification (x6) in comparison with classical stress-assisted variant selection.
4) The variant selection related to the TADA effect along the cross section of the lamellae was quantified by EBSD using the maximal work criterion. The microscopic variant selection profile calculated from the lattice distortion was found to fit well the predicted profile calculated from the macroscopic radius of curvature of the lamella.
5) After distortion, when the reverse transformation is induced by a high temperature annealing, the lamella comes back to its initial shape by a classical SME, which also confirms that the TADA effect results from a mechanism of variant selection.
6) The details of the mechanism are not yet fully understood. The degree of the phase transformation (first-order or second-order) should be clarified in order to build a physical model for the TADA effect.

Declaration of Competing Interest

The authors declare that they have no known competing financial interests or personal relationships that could have appeared to influence the work reported in this paper.

Acknowledgement

M. Larcher would like to acknowledge Dr A. Baur, M. St Jalme and R. Drissi Daoudi for their help and support. The authors gratefully acknowledge PX Group for the LMTM sponsorship. We also express our gratitude to the reviewers for their helpful comments.

Funding

This work was supported by the Innosuisse - Agence Suisse pour l'encouragement de l'innovation – [Grant No. 19242.1 PFIW-IW]; and the Swiss National Science Foundation (SNSF) [Grant No. 206021_182981 "Ultrafast EBSD System on a new SEM"].

Supplementary materials

Supplementary material associated with this article can be found, in the online version, at doi:10.1016/j.actamat.2020.07.064.

Appendices

A. Initial texture of the lamellae in the f.c.c. phase

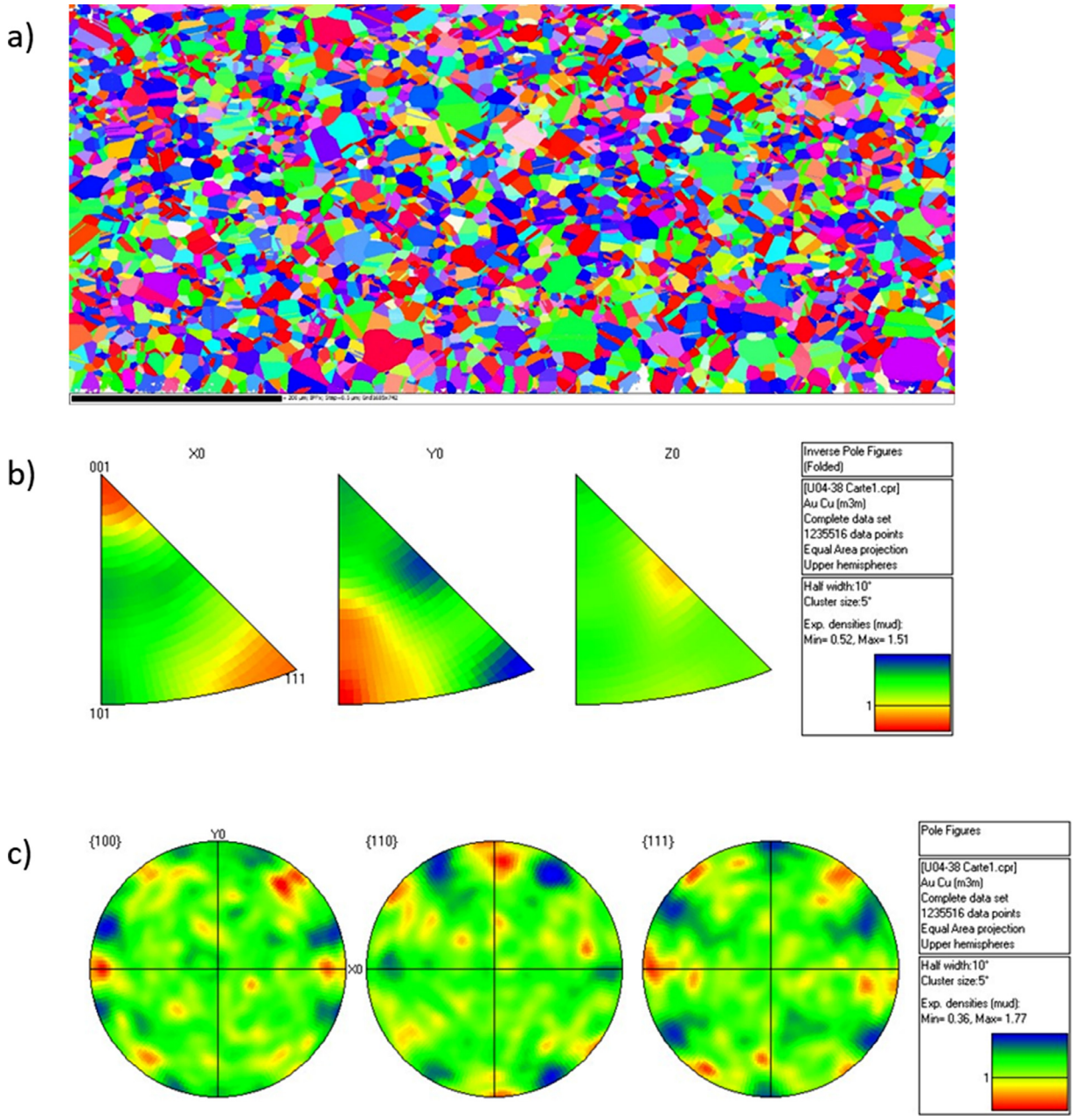

Fig. A.1. Initial lamella in the f.c.c. phase before stress application and before heat treatment. a) EBSD map of the f.c.c. phase in IPFx colors b) Inverse pole figures of the EBSD map c) Poles figures of the EBSD map. The maximal MUD (Multiple of Uniform Distribution) is of 1.77, which shows that the lamella is not textured.

B. EBSD full map of L60

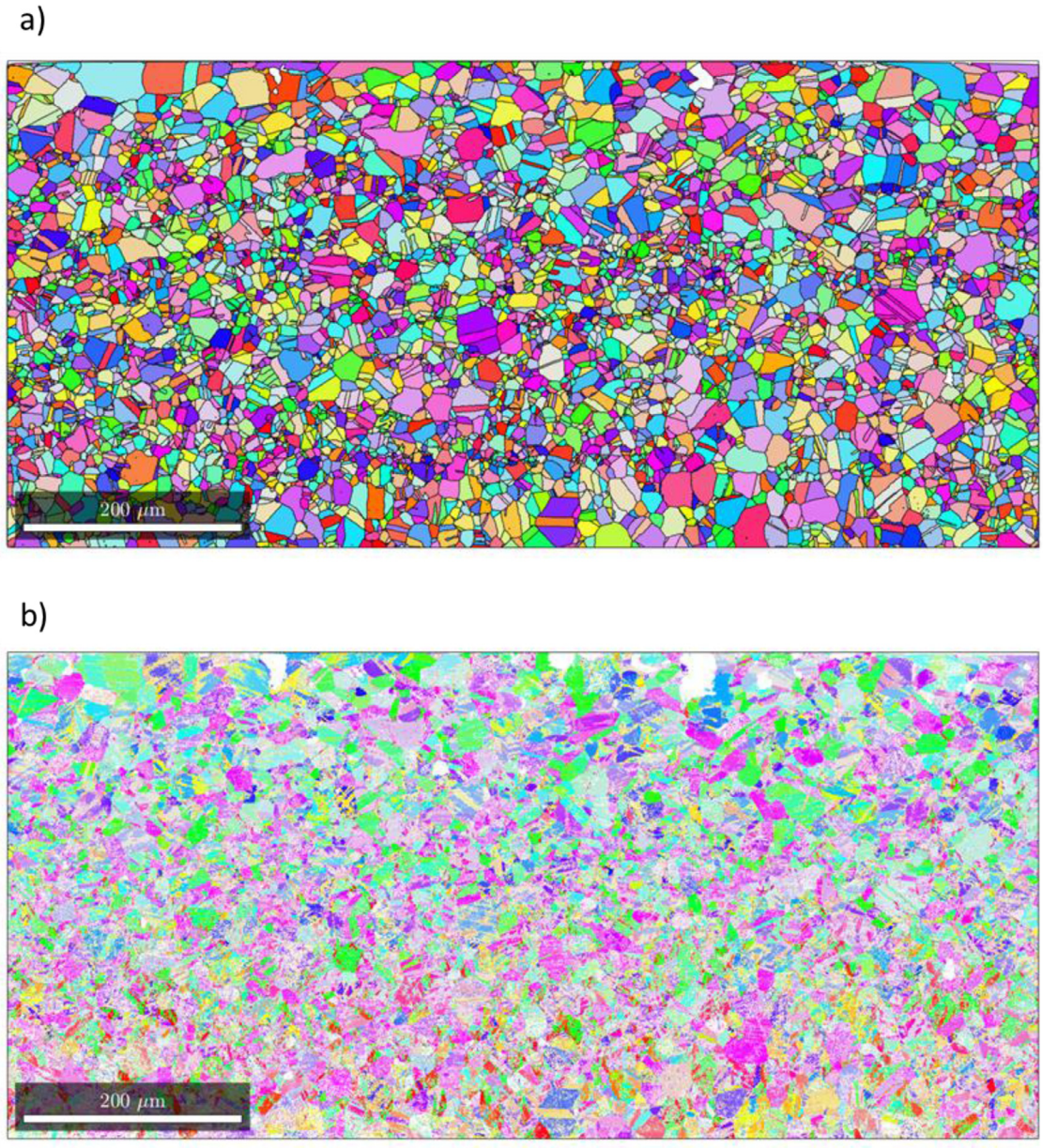

Fig. B.1. EBSD full map n°1 in the lamella L60 a) reconstructed f.c.c. parent grains b) f.c.t. domains in IPFx coloring.

C. EBSD full map of F60

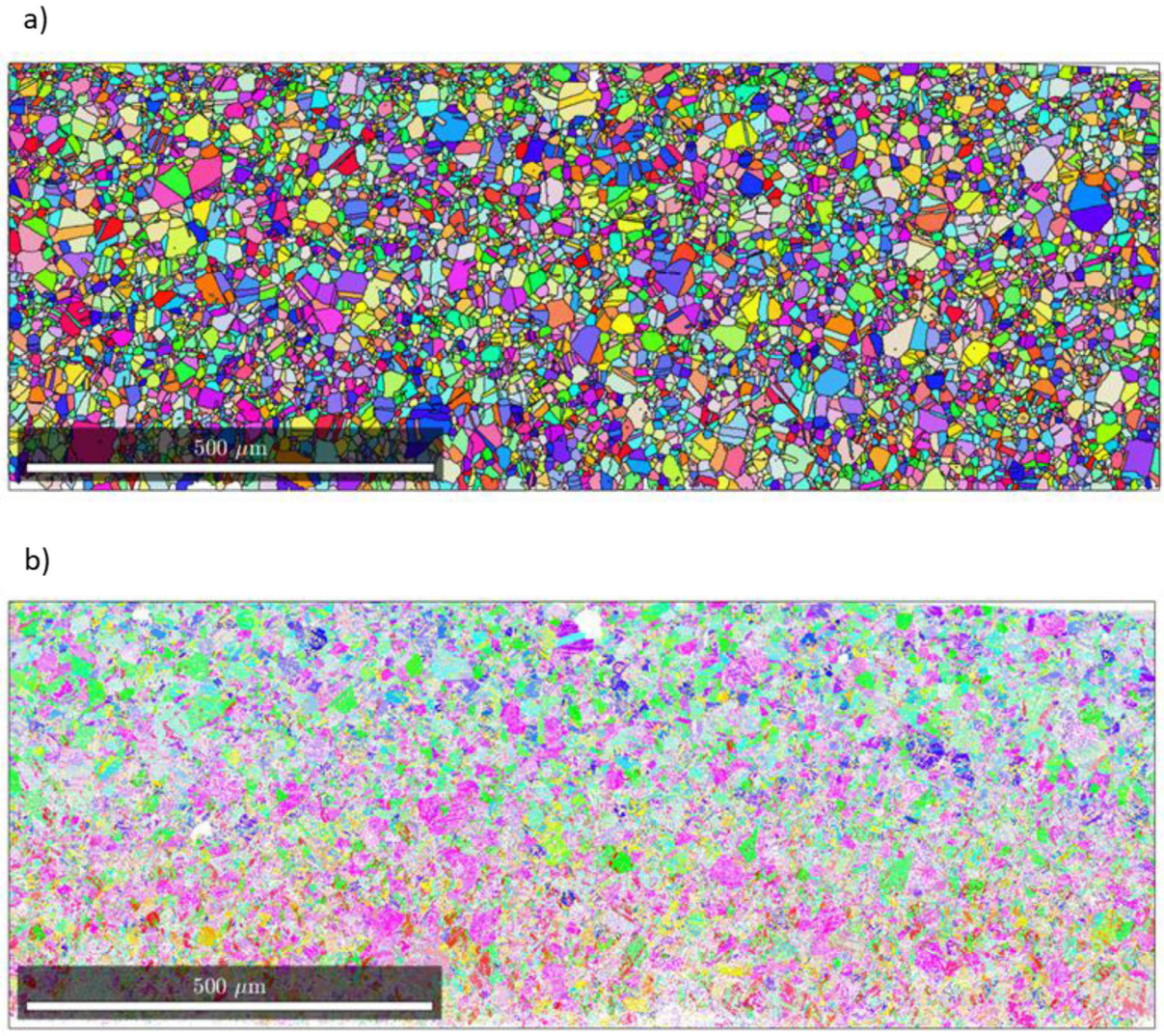

Fig. C.1. EBSD Map n°1 in the lamella F60 a) reconstructed f.c.c. parent grains b) f.c.t. domains in IPFx coloring.

References

[1] H. Okamoto, D.J. Chakrabarti, D.E. Laughlin, T.B. Massalski, The Au-Cu (Gold-Copper) system, Bull. Alloy Phase Diagr. 8 (1987) 454–474 https://doi.org/10.1007/BF02893155.

[2] G.C. Kuczynski, R.F. Hochman, M. Doyama, Study of the kinetics of ordering in the Alloy AuCu, J. Appl. Phys. 26 (1955) 871–878 https://doi.org/10.1063/1.1700094.

[3] M. Garcia-gonzalez, S. Van Petegem, N. Baluc, S. Hocine, M. Dupraz, F. Lalire, H. Van Swygenhoven, Enhanced precipitate growth at reduced temperatures during chemical ordering in deformed red gold alloys, Scr. Mater. 170 (2019) 129–133 https://doi.org/10.1016/j.scriptamat.2019.05.038.

[4] M. Hirabayashi, S. Weissmann, Study of CuAu I by transmission electron microscopy, Acta Metall. 10 (1962) 25–36 https://doi.org/10.1016/0001-6160(62)90183-9.

[5] V.S. Arunachalam, R.W. Cahn, Order-Hardening in CuAu, J, Mater. Sci. 2 (1967) 160–170 https://doi.org/10.1007/BF00549575.

[6] G. Van Tendeloo, S. Amelinckx, S.J. Jeng, C.M. Wayman, The initial stages of ordering in CuAu I and CuAu II, J. Mater. Sci. 21 (1986) 4395–4402 https://doi.org/10.1007/BF01106562.

[7] M. Ohta, T. Shiraishi, R. Ouchida, M. Nakagawa, S. Matsuya, Shape restoration effect associated with order–disorder transformation in equiatomic AuCu and AuCu–Ga alloys, J. Alloys Compd. 265 (1998) 240–248 https://doi.org/10.1016/S0925-8388(97)00307-1.

[8] K. Tanaka, K. Moriokaz, Shape memory characteristics in the L10–fcc order – disorder transformation of FePd, Philos. Mag 83 (2003) 1797–1806 https://doi.org/10.1080/1478643031000097124.

[9] K. Tanaka, Shape memory effect through L10-fcc order-disorder transition, MRS Proc. (2005) 359–364 https://doi.org/10.1557/PROC-842-S3.8.

[10] C.M. Wayman, Shape memory and related phenomena, Prog. Mater. Sci. 36 (1992) 203–224.

[11] K. Bhattacharya, Microstructure of martensite: why it forms and how it gives rise to the shape-memory effect, Oxford University Press, Oxford, 2003.

[12] K. Otsuka, C.M. Wayman, Shape Memory Materials, Cambridge, Cambridge, 1999.

[13] Z. Nishiyama, P Academic (Ed.), Elsevier, 1978 https://doi.org/10.1016/B978-0-12-519850-9.X5001-7.

[14] L.C.D. Fielding, The Bainite Controversy, Mater. Sci. Technol. 29 (2013) 383–399 https://doi.org/10.1179/1743284712y.0000000157.

[15] C.M. Wayman, in: Shape Memory Alloys, MRS Bull, 1993, pp. 49–56.

[16] P. Masek, A. Chmelik, V. Sima, A. Brinck, H. Neuhäuser, Microstructure processes induced by phase transitions in a CuAu alloy as studied by acoustic emission and optical cinematography, Acta Mater. 47 (1999) 427–434.

[17] S. Shimizu, S. Horiuchi, Fiber texture formed on transformation from disordered Fcc phase to ordered Fct phase under load, Metall. Trans. 1 (1970) 330–331.

[18] T. Ichitsubo, K. Tanaka, M. Nakamoto, T. Miyoshi, M. Koiwa, Effect of applied stress on ordering of FePd, in: Proc. Int. Conf. Solid-Solid Phase Transform, 1999, pp. 385–388.

[19] K. Tanaka, T. Ichitsubo, M. Koiwa, Effect of external fields on ordering of FePd, Mater. Sci. Eng. A. 312 (2001) 118–127.

[20] M.N.D. Larcher, C. Cayron, A. Blatter, R. Soulignac, R.E. Logé, Electron backscatter diffraction study of variant selection during ordering phase transformation in L10 -type red gold alloy, J, Appl. Crystallogr. 52 (2019) 1–12 https://doi.org/10.1107/S1600576719011890.

[21] A. Prince, G. Raynor, D. Evans, Phase Diagrams of Ternary Gold Alloys, Institute of metals, London, 1990.

[22] T. Shiraishi, M. Ohta, M. Nakagawa, R. Ouchida, Effects of small silver addition to AuCu on the AuCu I ordering process and age-hardening behaviours, J. Alloys Compd. 257 (1997) 306–312.

[23] A.M. El Araby, Y. Tanaka, K.-I. Udoh, K. Hisatsune, K. Yasuda, Coherent phase diagram of the AuCuPt section in the AuCuPt ternary system, J. Alloys Compd. 206 (1994) 217–224 https://doi.org/10.1016/0925-8388(94)90039-6.

[24] R.H. Luciano, T. Shiraishi, K.-I. Udoh, Y. Tanaka, K. Hisatsune, Microstructures and coherent phase diagram for the pseudobinary system (AuCu)1-xPdx with $x \leq 0.10$, J. Alloys Compd. 392 (2005) 142–148 https://doi.org/10.1016/j.jallcom.2004.08.108.

[25] K. Udoh, M. Ohta, K. Oki, K. Hisatsune, Phase diagram of AuCu-Ag pseudobinary alloy, J. Phase Equilib. 22 (2001) 306–311 https://doi.org/10.1361/105497101770338815.

[26] A. Baur, C. Cayron, R.E. Logé, Variant selection in Fe-20Ni-1.8C under bending, crystals. 8 (2018) 474. https://doi.org/10.3390/cryst8120474.

[27] R. Wolf, Electropolishing of gold and gold-rich alloys, Micron 8 (1977) 171–172 https://doi.org/10.1016/0047-7206(77)90021-8.

[28] C. Cayron, ARPGE: a computer program to automatically reconstruct the parent grains from electron backscatter diffraction data, J. Appl. Crystallogr. 40 (2007) 1183–1188 https://doi.org/10.1107/S0021889807048777.

[29] A.Y. Volkov, V.A. Kazantsev, Impact of the initial state on the structure and properties of the ordered CuAu alloy, Phys. Met. Metall. 113 (2012) 62–71 https://doi.org/10.1134/S0031918X12010127.

[30] T. Ichitsubo, M. Nakamoto, K. Tanaka, M. Koiwa, Effect of applied stress on fcc-L10 transformation of FePd single crystal, Mater. Trans. 39 (1998) 24–30.

[31] A. Shibata, T. Murakami, S. Morito, T. Furuhara, T. Maki, The origin of midrib in lenticular martensite, Mater. Trans. 49 (2008) 1242–1248 https://doi.org/10.2320/jinstmet.73.290.

[32] G. Borelius, On the equilibrium and kinetics of the order-disorder transformations in alloys, J. Inst. Met. 74 (1948) 17–31.

[33] J.L. O'Brien, G.C. Kuczynski, X-Ray study of the kinetics of ordering in AuCu, Acta Metall. 7 (1959) 803–806.

[34] R.A. Oriani, Thermodynamics of ordering alloys, II. The gold-copper system, Acta Metall. 2 (1954) 608–615 https://doi.org/10.1016/0001-6160(54)90196-0.

[35] R.L. Orr, J. Luciat-Labry, R. Hultgren, Energy of the order-disorder transformation in AuCu, Acta Metall. 8 (1960) 431–434 https://doi.org/10.1016/0001-6160(60)90029-8.

[36] Y. Tanaka, K.-I. Udoh, K. Hisatsune, K. Yasuda, Early stage of ordering in stoichiometric AuCu alloy, Mater. Trans. 39 (1998) 87–94.